

Detection of significant X-ray polarization from transient NS-LMXB XTE J1701–462 with IXPE and its implication on the coronal geometry

Kiran M. Jayasurya^{1*}, Vivek K. Agrawal¹ and Rwitika Chatterjee¹

¹Space Astronomy Group, ISITE Campus, U. R. Rao Satellite Centre, Bangalore, 560037, India

Accepted XXX. Received YYY; in original form ZZZ

ABSTRACT

In this paper, we performed a spectro-polarimetric analysis of the transient NS-LMXB XTE J1701 – 462 using *IXPE*, *NICER* and *NuSTAR* data during its 2022 outburst. We report significant detection of energy-dependent polarization in the X-ray signal from the source on 2022 September 29 in the 2 – 4 keV, 4 – 8 keV and 2 – 8 keV energy bands with a polarization degree of $3.9 \pm 0.3\%$, $5.5 \pm 0.6\%$ and $4.5 \pm 0.4\%$, respectively. The polarization angle in the overall 2 – 8 keV band was $\sim 143^\circ \pm 2^\circ$. The spectra were modelled using a combination of thermal emission from an accretion disc, Comptonized emission from a hot electron plasma (or corona) and a Gaussian line. From spectro-polarimetric analysis, the polarization degree due to the disc emission had an upper limit of $\sim 11.5\%$, and that of the Comptonized emission was constrained at $7.7 \pm 2.5\%$ (at the 3σ level). The results suggest that the Comptonized component probably originates from a spreading-layer/boundary-layer above the neutron star surface. IXPE observation of the source on 2022 October 8 does not show significant polarization which can be attributed to a weakening of the coronal Comptonized emission. The implication of these results are discussed.

Key words: accretion, accretion disks – polarization – X-rays: binaries – X-rays: individual: XTE J1701 – 462

1 INTRODUCTION

Low-mass X-ray binaries (LMXBs) consisting of a low-magnetic field neutron star accreting material from a low-mass companion star show intensity and spectral variations on time scales ranging from hours to months, and are divided into two sub-groups, Z-sources and atoll sources. The classification is based on their joint spectral and temporal nature and the shape of the path that they trace out in the Colour-Colour diagram (CCD) and hardness intensity diagram (HID, [Hasinger & van der Klis 1989](#)). The Z-sources trace out a ‘Z’-shaped track having three branches: horizontal branch (HB), normal branch (NB) and flaring branch (FB). The Z-sources are further classified into two sub-categories based on the extent of their HB and FB. The Cyg-like Z-sources have prominent HB and weak FB, and vice-versa for the Sco-like Z-sources.

XTE J1701 – 462 is a neutron star low-mass X-ray binary (NS-LMXB) discovered with the *All Sky Monitor (ASM) of the Rossi X-ray Timing Explorer (RXTE)* in January 2006 ([Remillard et al. 2006](#)) and it is the only known source till date that shows both Z-like and Atoll-like behaviour. The first 10 weeks of observations suggested that it was a transient Z-source, the first of its kind ([Homan et al. 2007](#)). During the initial high intensity phase, the source displayed Cyg-like behaviour and then evolved into a Sco-like Z-source as the count rate decreased ([Lin et al. 2009](#)). During the decay phase of the ~ 600 days outburst, the source displayed atoll-like behaviour. MAXI/GSC observations has revealed that the source entered a new outburst phase on 2022 September 6 ([Iwakiri et al. 2022](#)).

In general, a combination of a thermal component and a Comptonized emission component is used in modeling the X-ray spec-

tra of Z and atoll sources ([Di Salvo et al. 2000, 2001](#); [Agrawal & Sreekumar 2003](#); [Agrawal & Misra 2009](#); [Agrawal et al. 2023](#); [Tarana et al. 2008](#); [Piraino et al. 2000, 2007](#)). The thermal component is either described by a multi-colour disc (MCD) component from standard thin disc ([Mitsuda et al. 1984](#)) or a single-temperature blackbody (BB) originating from the boundary-layer/spreading-layer (BL/SL). The Comptonized emission is produced by scattering of soft seed photons in a hot electron plasma. The seed photons are supplied by either relatively cold accretion disc or the neutron star surface.

[Lin et al. \(2009\)](#) fitted the X-ray spectrum of XTE 1701-462 with a combination of two thermal components (BB+MCD) and a constrained broken power-law (CBPL) with break energy fixed at 20 keV. A combination of a Comptonized component (compTT in XSPEC) and disc emission (MCD) has also been used to describe the X-ray spectrum of the source ([Wang et al. 2014](#)). Z-sources are generally found in the soft spectral state (SS). In this state, the Comptonized component kT_e is found to be in the range of 2 to 5 keV and the spectrum shows small but systematic variations along the complete Z-track ([Di Salvo et al. 2000, 2001, 2002](#)).

In order to constrain the radiative processes at play, the accretion flow geometry and orbital inclination in LMXBs, polarization data in the X-ray band is extremely useful. Detailed polarimetric simulations have been performed for some of the basic configurations (slab, wedge and shell type) of corona in compact objects ([Gnarini et al. 2022](#); [Schnittman & Krolik 2010](#)). Some of the LMXBs are a prime target of the *Imaging X-ray Polarimetry Explorer (IXPE)*, a polarimetric mission launched on 2021 December 9 ([Weisskopf et al. 2022](#)). These observations are providing a better view of the physical processes and geometry of the putative corona in these systems. Recently, significant polarization has been detected in LMXBs

* E-mail: kiranmj@urisc.gov.in

like Cyg X-2 (Farinelli et al. 2023) and GX 9+9 (Chatterjee et al. 2023; Ursini et al. 2023) with IXPE, and Sco X-1 and Cyg X-2, the PA was found to be aligned with the normal to the disc plane suggesting hot electron plasma (Compton corona) situated above the transition or spreading layer. No significant polarization was detected in the atoll source GS 1826–238 (Capitanio et al. 2023) with IXPE, constraining the system inclination and coronal geometry.

In this paper, we report the detection of polarized X-ray signal from XTE J1701 – 462 using IXPE data. We discuss the implication of our results and suggest a possible accretion flow and corona geometry in the source.

2 OBSERVATIONS AND DATA ANALYSIS

2.1 IXPE

IXPE is a Gas Pixel Detector (GPD)-based soft X-ray imaging polarimeter (Soffitta et al. 2021; Weisskopf et al. 2022), comprising of a 4 m focal length Mirror Module Assembly focusing X-rays onto three polarization-sensitive detector units (DUs) in the 2 – 8 keV energy range. IXPE observed XTE J1701 – 462 on 2022 September 29 (ObsID 01250601; hereafter referred to as Epoch 1) and again on 2022 October 8 (ObsID 01250701; hereafter referred to as Epoch 2) for 46.2 ks and 46.4 ks of net exposure times respectively.

The processed IXPE Level-2 data¹ was analyzed using IXPEOBSIM v30.0.0 (Baldini et al. 2022). The source region was defined as a 60" circle and the background region as an annulus of 180" inner and 240" outer radii respectively, centered at the source's centroid intensity. The source and background event lists were extracted using the XPSELECT task, following which the PCUBE algorithm of XPBIN task was used to generate the polarization cubes. The PHA1, PHA1Q and PHA1U algorithms were used to generate the Stokes I, Q and U spectra respectively.

The polarization degree (PD) and polarization angle (PA) were determined using the model-independent PCUBE algorithm (Kislat et al. 2015) for the energy bands 2 – 4 keV, 4 – 8 keV and 2 – 8 keV. The algorithm assumes that the PD and PA are independent, but they are not so in reality, and hence the uncertainties are more appropriately represented by the contours of their joint measurement.

The results of our polarimetric analysis for both IXPE Epochs are described in Section 3.2. We also performed a spectro-polarimetric model-dependent fit (Strohmayr 2017) using XSPEC and the latest IXPE response files (v12).

2.2 NICER and NuSTAR

The Neutron Star Interior Composition Explorer (NICER) observed XTE J1701 – 462 on 2022 September 29 (ObsID 5203390122) for 2784 s of net exposure time. The cleaned event files were extracted using `nicer12` task which performs standard calibration and screening of the unfiltered data. The source and background spectra (in the 0.2 – 12 keV energy band) were generated using `nicer13-spect` task. The tasks were performed using NICER-DAS software v10 distributed with HEASOFT v6.31.1² and the latest CALDB.

The source was also observed by the Nuclear Spectroscopic Telescope Array (NuSTAR) on 2022 October 8 (ObsID 90801325002)

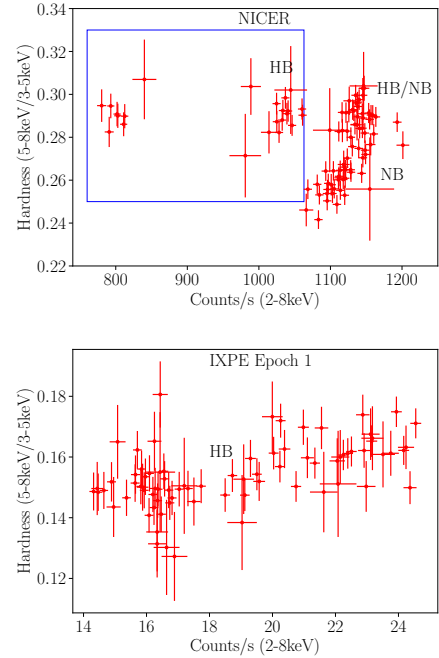


Figure 1. HIDs for NICER observation (top) and IXPE Epoch 1 (bottom, using the DU1). The blue box represents the region from which the NICER spectrum was extracted for analysis.

for a net exposure time of 12.2 ks. The unfiltered event files were calibrated and screened with the `nupipeline` task of NuSTARDAS (v1.9.7) using the latest CALDB files. The spectra were generated using the `nuproducts` task.

The NICER and NuSTAR quasi-simultaneous observations were considered for the spectro-polarimetric analysis of the IXPE Epoch 1 and Epoch 2 data respectively.

Since the NICER observation is close to Epoch 1, light curves in 3 – 5 keV, 5 – 8 keV and 2 – 8 keV bands were generated to create a HID of the source (Figure 1). The hardness was considered as the ratio of the counts in the 5 – 8 keV band to the 3 – 5 keV band, and the intensity was taken as the count rate in the 2 – 8 keV band. An HID was also created for the corresponding IXPE data using the DU1 in the same energy bands. The IXPE HID showed that the source was in the extended HB. Hence, we extracted the NICER spectrum in the HB (selection region is shown as a blue box in Figure 1).

During Epoch 2, part of the NuSTAR data overlapped with the IXPE observation period. A common good time interval (GTI) file was created by merging the GTI files of the NuSTAR and IXPE data using the `mgttime` task of FTOOLS. This file was then used to extract the NuSTAR spectra (for both FPMA and FPMB) for the spectral analysis.

Both NICER and NuSTAR spectra were re-binned to have minimum 25 counts per energy bin and the fitting was done in the 1.8 – 12 keV and 3 – 78 keV energy bands respectively.

3 RESULTS

3.1 Spectral Properties

The NICER spectrum (corresponding to the region marked

¹ Publicly available on the HEASARC Data Archive

² <http://heasarc.gsfc.nasa.gov/ftools>

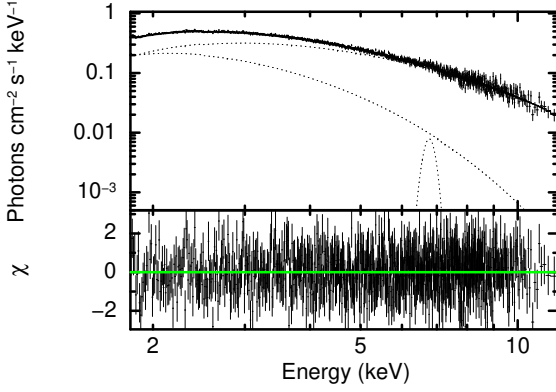


Figure 2. (Top panel) Unfolded *NICER* spectrum (corresponding to the region marked in Figure 1) of the source for Epoch 1, fitted with model 1. (Bottom panel) Residuals of the fit in units of σ .

in Figure 1) was fitted in XSPEC with three different models, which are widely used to describe NS-LMXB spectra: `tbabs*(diskbb+nthComp+gaussian)` (hereafter, model 1), `tbabs*(bbodyrad+diskbb+gaussian)` (hereafter, model 2) and `tbabs*(bbodyrad+nthComp+gaussian)` (hereafter, model 3).

In these models, `diskbb` component represents emission from a standard accretion disc (Mitsuda et al. 1984), `nthComp` describes the Comptonized emission from a hot electron plasma (see Zdziarski et al. 1996) and `bbodyrad` represents the single temperature blackbody emission from the neutron star surface. Model 1 represents a scenario where the soft emission comes from an accretion disc, the hard component from a corona which can have either spherical or slab-type geometry, and the seed photons for Comptonization originate from the neutron star surface. In model 2, the hotter component comes from the neutron star surface/BL, and cooler component originates from the accretion disc. Model 3 represents a scenario where the soft component comes from the neutron star surface/BL and the hard component from a corona having slab (or wedge) type geometry. The seed photons in this case are provided by the accretion disc. In all three scenarios, the iron emission line is modelled by a gaussian component and is believed to be produced by the reflection of coronal (in model 1 or 3) or BB (in model 2) radiation over the inner accretion disc. This reflection feature is usually associated with a broad continuum, an iron line and an absorption edge which are smeared due to relativistic effects.

All three models produced acceptable fits to the spectra and the best-fit parameters are tabulated in Table 1. The *NICER* spectrum fitted with model 1 is also shown in Figure 2. We also fit the *NuSTAR* spectra with these models multiplied by a `smedge` (smeared edge, Ebisawa 1991; Ebisawa et al. 1994) component, due to the presence of a weak reflection feature, resulting in better reduced chi-square values. The best-fit parameters are shown in Table 2.

3.2 Spectro-Polarimetric Properties

The polarization parameters derived from PCUBE for both IXPE Epochs are shown in Table 3. We note that the source shows significant polarization during Epoch 1, with PD of $3.89 \pm 0.36\%$, $5.52 \pm 0.60\%$ and $4.53 \pm 0.36\%$, (with a significance of 10.7σ , 9.1σ and 12.6σ respectively) for the 2–4, 4–8 and 2–8 keV energy bands respectively. The PA for the respective energy bands are $146^\circ \pm 3^\circ$, $140^\circ \pm 3^\circ$, and $143^\circ \pm 2^\circ$. For Epoch 2, we did not find significant polarization, with PD below the minimum detectable po-

Table 1. Best fit parameters for the *NICER* spectrum (for the region marked in Figure 1) for Epoch 1. N_H : Hydrogen column density; kT_{bb} : blackbody temperature; kT_{in} : inner disc temperature; Γ_{nth} : photon index; $kT_{s,nth}$: seed photon temperature for `nthcomp`; kT_e : electron plasma temperature; τ is the optical depth of the corona (assuming spherical geometry). N_{bb} , N_{diskbb} and N_{nth} are the normalizations for the `bbodyrad`, `diskbb` and `nthcomp` components respectively. E_l , σ_l , and EW are the center, width, and equivalent width of the Gaussian line respectively. F_{bb} , F_{diskbb} and F_{nth} are the unabsorbed fluxes in the 3–10 keV range for the `bbodyrad`, `diskbb` and `nthcomp` components respectively, in units of 10^{-9} ergs cm^{-2} s^{-1} . Uncertainties are quoted at the 1σ confidence range.

Parameter	Model 1	Model 2	Model 3
N_H (10^{22} cm^{-2})	1.7*	1.9*	1.9*
kT_{bb} (keV)	-	$2.4^{+0.5}_{-0.3}$	1.0 ± 0.1
N_{bb} (keV)	-	12^{+11}_{-7}	304^{+51}_{-34}
kT_{in} (keV)	0.89*	1.7 ± 0.1	-
N_{diskbb}	333^{+25}_{-33}	93^{+11}_{-12}	-
Γ_{nth}	$2.0^{+0.3}_{-0.2}$	-	$1.7^{+0.3}_{-0.2}$
kT_e (keV)	$2.3^{+0.4}_{-0.2}$	-	$2.2^{+0.2}_{-0.1}$
$kT_{s,nth}$ (keV)	$0.91^{+0.07}_{-0.08}$	-	0.65*
N_{nth}	$0.55^{+0.06}_{-0.04}$	-	1.8 ± 0.1
E_l (keV)	6.8 ± 0.1	6.8 ± 0.1	6.8 ± 0.1
σ_l (keV)	$0.16^{+0.15}_{-0.07}$	$0.15^{+0.14}_{-0.06}$	$0.16^{+0.16}_{-0.06}$
EW (eV)	24	23	24
τ	11 ± 3	-	7.7 ± 0.9
F_{diskbb}	0.9	8.9	-
F_{bb}	-	2.6	2.0
F_{nth}	10	-	9.5
χ^2/DOF	778/762	782/763	780/762

* Frozen at best fit value.

† Black body seed photons for model 1, disc seed photons for model 3

Table 2. Best fit parameters for the *NuSTAR* spectrum for Epoch 2. Parameter definitions, units and uncertainty levels are same as in Table 1. E_{smedge} and $f_{max,smedge}$ are the threshold energy and maximum absorption factor at the threshold energy, respectively, for the smeared edge component.

Parameter	Model 1	Model 2	Model 3
N_H (10^{22} cm^{-2})	2.0*	1.9*	2.1*
E_{smedge} (keV)	8.8 ± 0.1	8.8 ± 0.1	$8.8^{+0.1}_{-0.2}$
$f_{max,smedge}$	6.8 ± 0.8	7.1 ± 0.9	3.1 ± 0.7
kT_{bb} (keV)	-	2.5 ± 0.1	1.2 ± 0.1
N_{bb} (keV)	-	$2.1^{+0.4}_{-0.3}$	327 ± 10
kT_{in} (keV)	1.4 ± 0.1	1.6 ± 0.1	-
N_{diskbb}	225^{+40}_{-49}	150 ± 3	-
Γ_{nth}	4.6 ± 0.1	-	2.5 ± 0.1
kT_e (keV)	4.5*	-	2.7 ± 0.1
$kT_{s,nth}$ (keV)	1.4 ± 0.1	-	0.33*
N_{nth}	$0.10^{+0.03}_{-0.04}$	-	6.1 ± 0.3
E_l (keV)	6.5 ± 0.1	6.5 ± 0.1	6.5 ± 0.1
σ_l (keV)	0.25 ± 0.05	$0.25^{+0.05}_{-0.04}$	0.18 ± 0.04
EW (eV)	44	43	32
τ	2.6 ± 0.3	-	7.5 ± 0.4
F_{diskbb}	6.8	9.9	-
F_{bb}	-	0.5	5.4
F_{nth}	3.6	-	5.2
χ^2/DOF	793/725	789/726	776/725

* Frozen at best fit value.

larizations (MDP) at the 99% level in all the energy bands (see Table 3).

We also performed a model dependent spectro-polarimetric analysis by simultaneously fitting the source and background spectra for the different Stokes parameters (I, Q & U) in the different energy bands for Epoch 1. This was carried out for the three models described in Section 3.1, multiplied by a single `polconst` (e.g. `tbabs*polconst*(diskbb+nthComp+gaussian)`). The parameters were frozen to their best-fit values, leaving only the normaliza-

Table 3. Polarization parameters obtained using the PCUBE algorithm (for all 3 DUs combined) in different energy bands, for both IXPE Epochs. The uncertainties are reported at the 1σ level.

Epoch 1			
Parameter	2–4 keV	4–8 keV	2–8 keV
Q/I (%)	1.50 ± 0.36	1.04 ± 0.60	1.31 ± 0.36
U/I (%)	-3.58 ± 0.36	5.42 ± 0.60	-4.34 ± 0.36
PD (%)	3.89 ± 0.36	5.52 ± 0.60	4.53 ± 0.36
PA (°)	146 ± 3	140 ± 3	143 ± 2
Epoch 2			
Parameter	2–4 keV	4–8 keV	2–8 keV
PD (%)	0.51 ± 0.33	1.60 ± 0.58	0.83 ± 0.33
MDP99(%)	1.01	1.78	1.00

Table 4. Polarization parameters derived from the spectro-polarimetric fitting of the Stokes spectra of Epoch 1 in different energy bands, using model 1 (top) and model 2 (bottom). Uncertainties and upper limit are quoted at the 3σ level. See text for details.

Model 1					
Parameter	Single polconst			Multiple polconst*	
	2-4 keV	4-8 keV	2-8 keV	diskbb	nthcomp
PD (%)	4.05 ± 1.13	5.89 ± 1.63	4.70 ± 0.93	< 11.5	7.72 ± 2.47
PA (°)	145 ± 8	144 ± 8	145 ± 5	unconstrained	139 ± 9
χ^2/DOF	360/434	920/884	1442/1334	1423/1332	
Model 2					
Parameter	Single polconst			Multiple polconst*	
	2-4 keV	4-8 keV	2-8 keV	bbbodyrad	diskbb
PD (%)	4.05 ± 1.11	5.88 ± 1.62	4.69 ± 0.92	unconstrained	3.33 ± 1.73
PA (°)	145 ± 8	144 ± 8	144 ± 6	unconstrained	153 ± 14
χ^2/DOF	364/434	822/884	1231/1334	1220/1330	

Fitted in the 2–8 keV range

tion and polarization parameters to vary freely (Farinelli et al. 2023; Capitanio et al. 2023). The results of the spectro-polarimetric fit with model 1 are shown in Table 4. Figures 3a and 3b show the 1σ , 2σ , and 3σ contours of this fit in the 2–4, 4–8 and 2–8 keV bands. The polarization parameters and contours, although not fully coincident, are in good agreement with those from PCUBE.

We also carried out the spectro-polarimetric analysis of Epoch 1 data with multiple polconst, one multiplied with each component (e.g. `tbabs*(polconst*diskbb+polconst*nthComp+gaussian)`). The gaussian component is generally not expected to be polarized and hence, we have not multiplied polconst to it. For model 1, the polarization of nthcomp was well-constrained with PD of $7.7 \pm 2.5\%$ and PA of $139 \pm 9^\circ$. However, the PD of diskbb was unconstrained with a 3σ upper limit of 11.5%. The fit statistic (χ^2/DOF) was found to be 1442/1332. The results for model 1 are shown in Table 4 and Figure 3c.

For model 2 with multiple polconst, the fit statistic was at 1220/1330 with diskbb PD = $3.3 \pm 1.7\%$ & PA = $153^\circ \pm 14^\circ$ (at the 3σ level). However, the PD of the bbbodyrad could not be constrained. For model 3, the PD was unconstrained for both bbbodyrad and nthcomp components, and the fit statistic was slightly worse at 1661/1330.

4 DISCUSSION

Though detailed investigations of spectral and temporal properties of bright LMXBs have been carried out in the past decades, radiative

processes and nature of accretion flow in these systems still remain uncertain. Hence, polarization measurements can play a crucial role in unfolding the nature of accretion flow, emission mechanisms in these sources.

In this work, we report the significant detection of X-ray polarization for IXPE Epoch 1 data as detailed in Section 3. We also carried out model dependent analysis of spectro-polarimetric data using three different models, which provide good fit to the IXPE Epoch 1 data. However, model 3 does not constrain the PD of the individual components. Hence, this model could be excluded from consideration. Model 2 gives low value of PD ($3.3 \pm 1.7\%$) for the disc component and that of the black body component could not be constrained. The simulations carried out by Schnittman & Krolik (2009) suggest that for direct emission from the accretion disc in the thermal state, the PD decreases with energy and the PA remains constant (see Figure 2 in the cited paper). However, in our case, the PD increases with energy (Table 4), suggesting that a scenario where polarization arises from a ‘dominant’ accretion disc may not represent the emission spectrum of the source. It should be noted that the best-fit inner disc and blackbody temperatures are unusually high for model 2.

The application of model 1 to spectro-polarimetric data gives PD= $7.7 \pm 2.5\%$ and PA= $139 \pm 9^\circ$ for the Comptonized component. The polarization fraction for disc component could not be constrained (see Table 4). The spectral parameters obtained by NICER analysis suggests that during Epoch 1, the source was in the soft state. The presence of iron line with equivalent width < 30 eV, suggests signature of weak reflection. Hence, the orbital inclination of the system is probably close to 75° (Lin et al. 2009).

The simulations carried out by Gnarini et al. (2022) for NS-LMXBs predict that the PD in these sources is $< 5\%$. However, the observed PD of the Comptonized component is higher than this. There may be two reasons for this discrepancy. Firstly, their simulations do not consider reflection from the disc which may have resulted in a lower PD. Secondly, the narrow energy band of IXPE does not allow for detailed spectro-polarimetric modeling of the reflection component. Hence, modeling the data in XSPEC with a disc and Comptonized component may result in the polarization due to reflection to be attributed to that due to Comptonization (Farinelli et al. 2023). The spectro-polarimetric analysis shows that the best-fit model consists of emission from a MCD and a Comptonized corona. In this scenario, the Comptonized component is likely to originate from a spreading layer or a boundary layer above the NS surface.

During IXPE Epoch 2, we do not detect significant polarization from the source. To investigate this, we modelled the NuSTAR spectrum overlapping with the IXPE observation, using all three models. Using model 1, we find that the corona has become hotter from $kT_e = 2.3$ to $kT_e = 4.5$ keV and its optical depth has reduced from $\tau = 11$ to $\tau = 2.6$. In the other scenario (model 2), the inner disc temperature and blackbody temperature remain nearly same across the two epochs. However, the disc component became stronger and the harder blackbody component became weaker during Epoch 2.

We note that for model 1, the flux of the Comptonized component has weakened compared to Epoch 1 by a factor of ~ 2.9 , whereas that of the disc component has increased by a factor of ~ 7.4 . As suggested by previous observations of bright LMXBs and present spectro-polarimetric analysis of Epoch 1 data, the disc emission is weakly or probably not polarized (Farinelli et al. 2023; Chatterjee et al. 2023). Further, a weak corona is not expected to produce high polarization. Hence, the polarization from the source during Epoch 2 may have fallen below the polarization sensitivity of IXPE.

The same IXPE observations of XTE J1701–462 were analyzed

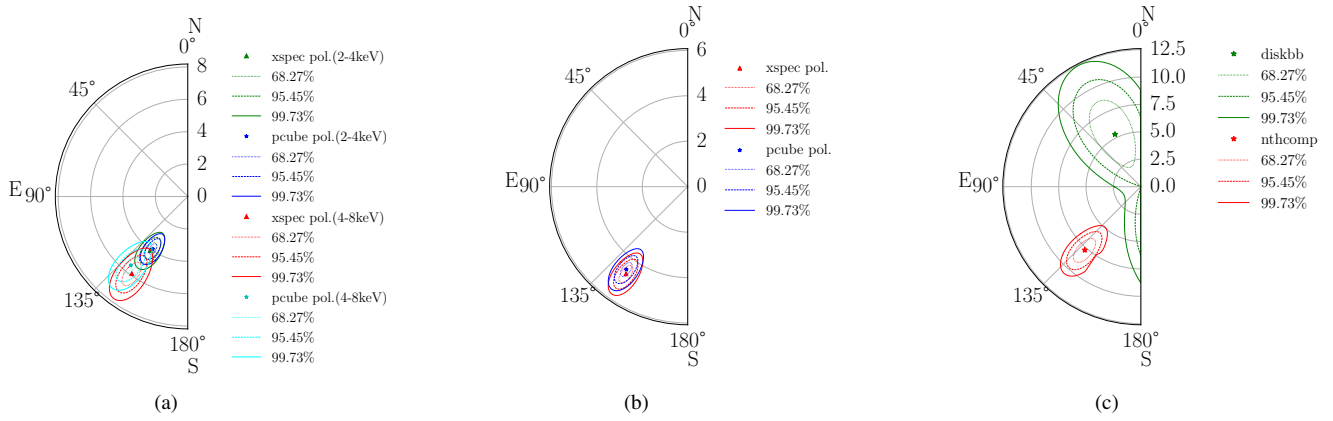


Figure 3. Polarization contours derived from: (a) XSPEC (triangle) and PCUBE (star) in the 2–4 keV (green & blue) and 4–8 keV (red & cyan) energy bands; (b) XSPEC (red) and PCUBE (blue) over the 2–8 keV energy range; (c) XSPEC using individual `polconst` for `diskbb` (green) and `nthcomp` (red) respectively in the 2–8 keV energy range. In all three panels, the *IXPE* spectra have been fitted with the best-fit *NICER* parameters using model 1 for Epoch 1, and the 1σ (dotted), 2σ (dashed) and 3σ (solid) contours are shown. See text for details.

in parallel to this work by Cocchi et al. (2023). We note that the authors of the publication have used only *IXPE* data, whereas we have used quasi-simultaneous *NICER* and *NuSTAR* data for the spectral fitting. Cocchi et al. (2023) were admittedly unable to model the *IXPE* spectra (due to its narrow energy band) with a Comptonized emission component which is a better way to describe the wide band spectrum of the source. We have used a Comptonized component in model 1 and model 3 for our analysis. We also note that the moderate energy resolution of the *IXPE* GPD cannot resolve the Gaussian emission line seen in the *NICER* and *NuSTAR* spectra and is therefore not considered in their spectral fitting.

Although our polarimetric results are consistent with that reported in Cocchi et al. (2023), there is a discrepancy in the spectral fits. We attribute this to the fact that the authors have done the spectral fitting in the narrow 2–8 keV energy band of *IXPE*, resulting in higher N_H , and lower blackbody and inner disc temperatures. To test this, we performed spectral analysis using model 2 (without the Gaussian component) for the *NICER* and *NuSTAR* data in the 2–8 keV and 3–8 keV band, respectively, by fixing N_H as reported in Cocchi et al. (2023). This exercise resulted in spectral fit parameters similar to theirs. We note that spurious line edges not considered in the *NICER* RMF and ARF could have slightly distorted the spectrum and also contributed to the discrepancy in the spectral results. However, the *NuSTAR* data also gives similar values of inner disc temperature and blackbody temperature suggesting that the discrepancy cannot be attributed only to the artifacts in the *NICER* response. We also found that the spectral fit parameters derived using only *IXPE* data are unable to explain the higher energy spectra of *NuSTAR* (> 10 keV). However, our spectro-polarimetric results as well as those of Cocchi et al. (2023) can be explained by Comptonized emission, probably originating from a spreading-layer/boundary-layer above the neutron star surface.

A radio jet like emission in the north-south direction had been observed in this source (Fender et al. 2007). However, recent MeerKAT and ATCA observations of its new outburst suggest that the large-scale jet are probably background radio galaxies (Gasealahwe et al. 2023). Hence, we cannot comment about the orientation of PA of the polarized X-ray signal with respect to the symmetry axis.

ACKNOWLEDGMENTS

The authors thank the anonymous reviewer for providing valuable suggestions to improve the quality of the manuscript. The authors also thank GH, SAG; DD, PDMSA and Director, URSC for encouragement and continuous support to carry out this research.

This research used data products provided by the *IXPE* team (MSFC, SSCC, INAF, and INFN) and software tools distributed by the High-Energy Astrophysics Science Archive Research Center (HEASARC), at NASA Goddard Space Flight Center (GSFC).

DATA AVAILABILITY

IXPE, *NICER* and *NuSTAR* data underlying this work are available at High Energy Astrophysics Science Archive Research Center (HEASARC) facility, located at NASA-Goddard Space Flight Center.

REFERENCES

- Agrawal V. K., Misra R., 2009, *MNRAS*, **398**, 1352
 Agrawal V. K., Sreekumar P., 2003, *MNRAS*, **346**, 933
 Agrawal V. K., Nandi A., Katoch T., 2023, *MNRAS*, **518**, 194
 Baldini L., et al., 2022, *SoftwareX*, **19**, 101194
 Capitanio F., et al., 2023, *ApJ*, **943**, 129
 Chatterjee R., Agrawal V. K., Jayasurya K. M., Katoch T., 2023, *MNRAS*, **521**, L74
 Cocchi M., et al., 2023, *A&A*, **674**, L10
 Di Salvo T., et al., 2000, *ApJ*, **544**, L119
 Di Salvo T., Robba N. R., Iaria R., Stella L., Burderi L., Israel G. L., 2001, *ApJ*, **554**, 49
 Di Salvo T., Robba N., Stella L., 2002, *Mem. Soc. Astron. Italiana*, **73**, 1082
 Ebisawa K., 1991, PhD thesis, JAXA, Institute of Space and Astronautical Science
 Ebisawa K., et al., 1994, *PASJ*, **46**, 375
 Farinelli R., et al., 2023, *MNRAS*, **519**, 3681
 Fender R. P., Dahlem M., Homan J., Corbel S., Sault R., Belloni T. M., 2007, *MNRAS*, **380**, L25
 Gasealahwe K. V. S., et al., 2023, *MNRAS*,
 Gnarini A., Ursini F., Matt G., Bianchi S., Capitanio F., Cocchi M., Farinelli R., Zhang W., 2022, *MNRAS*, **514**, 2561

- Hasinger G., van der Klis M., 1989, *A&A*, **225**, 79
- Homan J., et al., 2007, *ApJ*, **656**, 420
- Iwakiri W., et al., 2022, *The Astronomer's Telegram*, **15592**, 1
- Kislat F., Clark B., Beilicke M., Krawczynski H., 2015, *Astroparticle Physics*, **68**, 45
- Lin D., Remillard R. A., Homan J., 2009, *ApJ*, **696**, 1257
- Long X., et al., 2022, *ApJ*, **924**, L13
- Mitsuda K., et al., 1984, *PASJ*, **36**, 741
- Piraino S., Santangelo A., Kaaret P., 2000, *A&A*, **360**, L35
- Piraino S., Santangelo A., di Salvo T., Kaaret P., Horns D., Iaria R., Burderi L., 2007, *A&A*, **471**, L17
- Remillard R. A., Lin D., ASM Team at MIT NASA/GSFC 2006, *The Astronomer's Telegram*, **696**, 1
- Schnittman J. D., Krolik J. H., 2009, *ApJ*, **701**, 1175
- Schnittman J. D., Krolik J. H., 2010, *ApJ*, **712**, 908
- Soffitta P., et al., 2021, *The Astronomical Journal*, **162**, 208
- Strohmayer T. E., 2017, *ApJ*, **838**, 72
- Tarana A., Bazzano A., Ubertini P., 2008, *ApJ*, **688**, 1295
- Ursini F., et al., 2023, *A&A*, **676**, A20
- Wang Y. N., Lei Y. J., Ding G. Q., Qu J. L., Ge M. Y., Zhang C. M., Chen L., Ma X., 2014, *MNRAS*, **440**, 3726
- Weisskopf M. C., et al., 2022, *Journal of Astronomical Telescopes, Instruments, and Systems*, **8**, 026002
- Zdziarski A. A., Johnson W. N., Magdziarz P., 1996, *MNRAS*, **283**, 193

This paper has been typeset from a $\text{\TeX}/\text{\LaTeX}$ file prepared by the author.